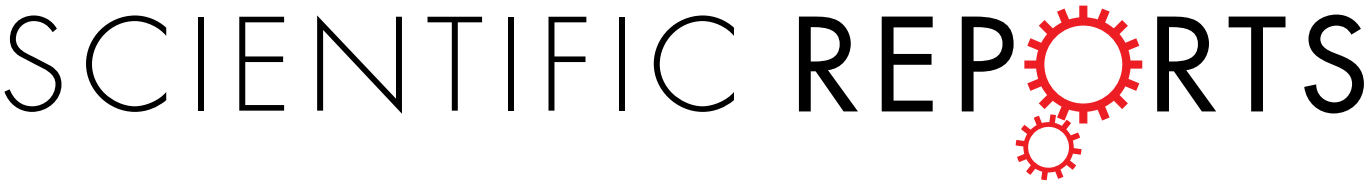

OPEN

# In-plane direct current probing for spin orbit torque-driven effective fields in perpendicularly magnetized heavy metal/ferromagnet/oxide frames

Received: 10 April 2018
Accepted: 10 July 2018
Published online: 23 July 2018

Seungmo Yang[1], Jinhyung Choi[1], Junghoon Shin[1], Kapsoo Yoon[1], Jungyup Yang[2] & JinPyo Hong[1]

**Electrical manipulation of magnetization states has been the subject of intense focus as it is a long-standing goal in the emerging field of spintronics. In particular, torque generated by an in-plane current with a strong spin-orbit interaction shows promise for control of the adjacent ferromagnetic state in heavy-metal/ferromagnet/oxide frames. Thus, the ability to unlock precise spin orbit torque-driven effective fields represents one of the key approaches in this work. Here, we address an in-plane direct current measurement approach as a generic alternative tool to identify spin orbit torque-driven effective fields in a full polar angle range without adopting the commonly used harmonic analyses. Our experimental results exhibited a strongly polar angular dependency of the spin orbit torque-driven effective fields observed from Ta or W/CoFeM/MgO frames.**

Recently, intentional manipulation of magnetization dynamics through the electric fields and current continues to be of significant interest from a fundamental perspective and for spintronic technologies. In particular, the in-plane current-driven spin orbit interaction (SOI) phenomenon, which is the so called spin-orbit torque (SOT), has garnered considerable interest for controlling magnetization in the adjacent ferromagnet. Electric currents in large SOI materials can induce a non-zero spin current or spin accumulation in a direction perpendicular to the charge flow via a conversion between electron spin and linear momentum, which can exert torque on the magnetization in the adjacent ferromagnets. A variety of works have been published on the nature of the SOT-related magnetic dynamics including magnetization switching[1–4], logic operations[5], and domain-wall motion[6,7] by considering two dominant mechanisms. One is the spin Hall Effect (SHE) arising from bulk materials with a large SOI (heavy metal layer)[8], and the other is the Rashba effect, which occurs at the interface between the heavy metal (HM) layer and ferromagnetic (FM) layer[9,10]. However, while both dynamics can provide two effective magnetic torques, which are commonly called the field-like torque ($\overrightarrow{T_f} \sim T_f \hat{M} \times \overrightarrow{\sigma}$) and the damping-like torque ($\overrightarrow{T_d} \sim T_d \hat{M} \times (\hat{M} \times \overrightarrow{\sigma})$), the relative magnitude and direction of $T_f$ and $T_d$ vary strongly depending on the stack configuration, the choice of HM, and oxidation degree[1,11]. In addition, previous studies have shown that the $T_f$ is mainly induced by the Rashba effect, while the $T_d$ is mostly governed by the spin Hall effect[12].

To date, numerous studies have also reported the successful determination of each effective magnetic field by means of diverse analysis approaches, such as field-current equivalence[13] and harmonic analysis[11,12,14]. However, the experimentally observed torque components ($T_f$ and $T_d$) evaluated even in the same structural frames exhibited distinct measurement or analysis dependence. For instance, Chen *et al.*[15] reported that the $T_f$ is nearly three times larger than the $T_d$, while Liu *et al.*[3] presented a large SHE-induced torque in Ta/CoFeB/MgO with a perpendicular magnetic anisotropy (PMA) feature. Furthermore, the suggested two underlying physics for spin-orbit torque (that is, the Rashba effect and SHE) cannot explain several reported phenomena, such as the influence of oxygen bonding state[1] and polar angle of magnetization[15]. Thus, the ability to identify each individual torque

[1]Novel Functional Materials and Device Laboratory, Research Institute of Natural Science, Department of Physics, Hanyang University, Seoul, 133-791, Korea. [2]Department of Physics, Kunsan National University, Kunsan, South Korea. Correspondence and requests for materials should be addressed to J.H. (email: jphong@hanyang.ac.kr)

component with their precise magnitudes and to establish a firm understanding of their physical origins remain key steps toward extending the use of these materials in emerging spintronic applications.

A unique concept in this work is the use of an in-plane direct current (DC) source as an independent tool for the determination of two current-induced effective magnetic fields in the representative HM/CoFeB/MgO stacks without the need for the commonly used harmonic measurement technologies. Several groups have already reported DC current technique to calibrate the SOT effective fields, our work shows some uniqueness compared the previous works. M. Kawaguchi *et al.*[16] reported two components of current-induced SOT along the y-axis (transverse field in the paper) and the z-axis (perpendicular field in the paper) for especial in-plane magnetic easy axis films. This approach might not be effective to the PMA-based frames. As is well-known, the PMA-based frames have widely been the focus of immense interest for the device applications and academic research. Second, J. Han *et al.*[17] also addressed the quantitative calibration of SOT using DC current-based analysis in PMA-based topological insulator frames. However, this work has considered only damping-like torque in the analysis: For example, only $H_z$ field was considered by employing the dominant current-induced switching along the z-axis. Thus, the uniqueness of our work serves to provide the approach for the determination of two separated spin torque components including Field-like torque and Damping-like torque in PMA-based frames.

We address the individual in-plane DC-induced SOT effective fields in both Ta and W-based HM/CoFeB/MgO stacks through control of various symmetry features. In particular, the dependence of the DC-induced effective magnetic fields on the magnetization polar angle (θ) in a full θ range was extensively evaluated, along with quantitative reliability tests afforded by the previously reported analysis approaches, including the field balance and energy equilibrium equations. An interfacial spin transparency concept that can occur at the HM/FM/oxide interface is briefly described based on the experimental findings.

## Results and Discussion

Figure 1a shows an optical microscope image of the fabricated Hall device with a 10 μm width. A more detailed description of the fabrication process is given in the Methods section. The sample stacks used have the structure of Si/$SiO_2$ (200)/HM (5)/CoFeB (1.2)/MgO (1)/Ta (3) (thicknesses in nanometers) and were post-annealed at a moderate temperature, where two different annealing temperatures are chosen for 250 °C for Ta and 350 °C for W HMs. Hereafter, the Ta-based sample is referred to as 'Sample A,' and the W-based sample is 'Sample B'. All samples exhibit typical PMA features due to the presence of interface anisotropy at CoFeB/MgO that is attributed to the hybridization of Fe 3d and O 2p orbitals[18] after the annealing process (see Supplementary Information 3). Figure 1b and c illustrate the DC source-driven SOT effective magnetic fields in the presence of an applied magnetic field ($H_{ext}$), along with the definition of the coordinate system. The current-induced effective magnetic fields have two components: the field-like effective field ($H_f$) and the damping-like effective field ($H_d$), which are defined by $\overrightarrow{H_f} \equiv T_f\overrightarrow{\sigma}$, $\overrightarrow{H_d} \equiv T_d(\hat{M} \times \overrightarrow{\sigma})$ from the two torque relations $\overrightarrow{T_f} = T_f\hat{M} \times \overrightarrow{\sigma}$ and $\overrightarrow{T_d} = T_d\hat{M} \times (\hat{M} \times \overrightarrow{\sigma})$. Two separate measurement schemes were introduced with the enlarged figures (right figures). One is the parallel measurement scheme (left of Fig. 1b), and the other is the perpendicular measurement scheme (left of Fig. 1c). In both schemes, the $H_{ext}$ with a tilting angle θ = 85° from vertical is swept in a wide range to maintain a single domain state during magnetization switching. In the parallel scheme, DC current ($I_{dc}$) with a magnitude of ±0.5 mA was injected along the x-axis and $H_{ext}$ were applied in the x-z plane with $\theta_H = 85°$, while the $H_{ext}$ was applied in the y-z plane with $\theta_H = 85°$ with the current flow along the x-axis for the perpendicular scheme. The enlarged figures (rights) of Fig. 1b and c also depict the key concept of magnetization tilting upon application of positive and negative $\pm I_{dc}$ in both schemes. For zero current ($I_{dc} = 0$), the direction of a magnetization vector ($\overrightarrow{M}$) in an FM layer is placed at the equilibrium position ($\theta_0$, $\varphi_0$) and is parallel to the sum of only two magnetic fields: $\overrightarrow{H_0}(\equiv \overrightarrow{H_{an}} + \overrightarrow{H_{ext}})$, where the anisotropic field ($\overrightarrow{H_{an}}$) and external field (..). Both magnetic parameters can be determined experimentally. When the $I_{dc}$ is applied through either an HM layer or an FM layer, the current-induced torque will allow for magnetization tilting of the FM layer toward the new equilibrium position (θ, $\varphi$) from the equilibrium position ($\theta_0$, $\varphi_0$). That is, an $I_{dc}$ sign with a finite amplitude leads to relative magnetization tilting with an amplitude of Δθ from the equilibrium state. Note that, in this analysis, the variations in the polar and azimuthal angles of magnetizations (Δθ, Δφ) mainly originate from the SOTs induced by the application of $I_{dc}$ because of the relatively small magnitude of the current-generated Oersted magnetic field (0.314 Oe, See Supplementary Information 9). In this regard, an $I_{dc}$-induced variation in magnetization establishes the experimental difference in the total Hall signal ($R_H$) observed in both schemes. Thus, tailoring the Δθ and Δφ upon application of $I_{dc}$ is a crucial step for determining the individual current-induced effective magnetic fields. Here, two measurement schemes are chosen to separately determine each individual $\overrightarrow{H_f}$ and $\overrightarrow{H_d}$. In the two schemes, the injection of an identical current (x-axis) is supposed to create the same direction of $\overrightarrow{H_f}$ (always along the y-axis) with the same magnitude due to the presence of the same spin polarization ($\overrightarrow{\sigma}$), which is one parameter for the exchange interaction with the magnetization ($\overrightarrow{M}$) under the Rashba effect-related torque. That is, the $\overrightarrow{H_f}$ ($\overrightarrow{H_f} \sim \overrightarrow{\sigma}$) is independent of the direction of magnetization. However, as the $\overrightarrow{H_d}$ may arise mainly from the spin current created by the SHE through the spin transfer torque (STT) phenomenon, the $\overrightarrow{H_d}$ ($\overrightarrow{H_d} \sim \overrightarrow{M} \times \overrightarrow{\sigma}$) relies on the initial magnetization direction. Thus, our work is hereafter discussed based on the simplest assumption in which the Δθ in a parallel scheme is only given by the $\overrightarrow{H_d}$ in the x-z plane, and the Δθ in a perpendicular scheme is only governed by the $\overrightarrow{H_f}$ in the y-z plane. That is, the separate determination of Δθ in the two schemes serves to determine the strengths of each $\overrightarrow{H_f}$ and $\overrightarrow{H_d}$. This is a key concept in the application of $\pm I_{dc}$ without adopting the commonly used harmonic analyses.

Considering the above concept, Fig. 2a and d show plots of the representative Hall resistance signal $R_H$ of Sample A as a function of $\overrightarrow{H_{ext}}$ upon the same magnitude of positive (red) and negative (blue color) $I_{dc}$ for both

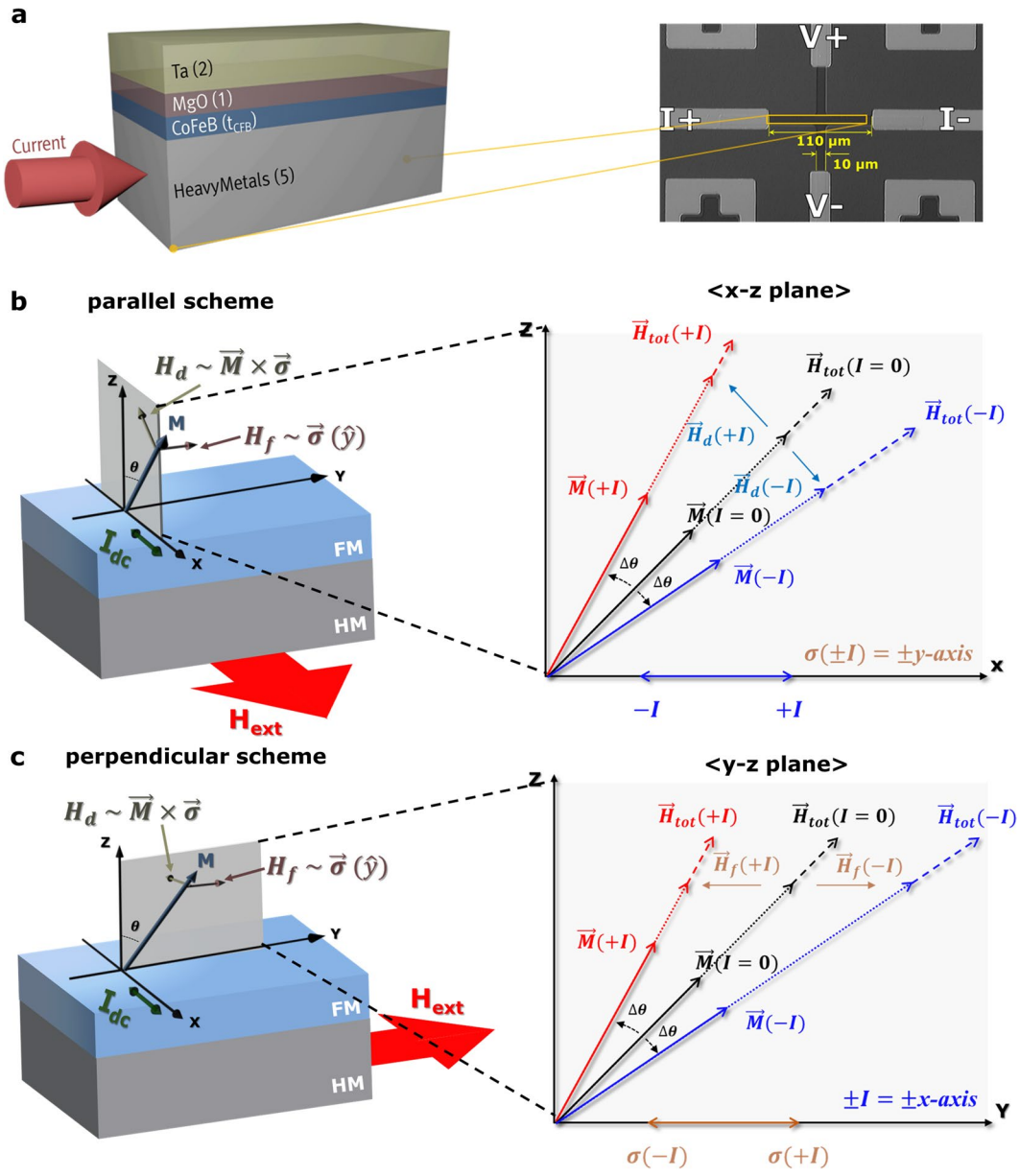


**Figure 1.** Schematics of sample stacks and individual current-induced effective fields provided by DC application. (**a**) Sample architecture (Left) and an optical image of the Hall bar device (Right). The current-induced effective field illustrations for individual SOT components ($H_d$ & $H_f$) in the presence of $H_{ext}$ (**b**) parallel and (**c**) perpendicular to the direct current $I_{dc}$ sources. Enlarged figures of (**b** and **c**) indicate significant shifts (red and blue colors) in the magnetization directions from the equilibrium state in the presence of the positive and negative DC sources, thereby ensuring a direct estimate of the individual $H_d$ & $H_f$ in z-x and z-y planes that depend on the parallel and perpendicular schemes, respectively.

parallel (Fig. 2a) and perpendicular (Fig. 2d) schemes, respectively, where the magnitude of the applied $I_{dc}$ is ±0.5 mA. As depicted above, the insets of Fig. 2a,d clearly show the distinct dependence of $R_H$ on the direction of $I_{dc}$; that is, $R_H$ increased for a positive $I_{dc}$ (red color) and decreased for a negative $I_{dc}$ (blue color). Thus, to identify the observed $R_H$ by the application of $I_{dc}$, three possible contributions to the $R_H$ curve were assumed as a first step as follows:

$$R_H(I_{dc}) = R_{OHE}(I_{dc}) + R_{AHE} \cdot \cos\theta(I_{dc}) + R_{PHE} \cdot \sin^2\theta(I_{dc}) \cdot \sin 2\varphi(I_{dc}) \quad (1)$$

where θ is the polar angle, $\varphi$ is the azimuthal angle of the magnetization, and $R_{AHE}$ and $R_{PHE}$ are the anomalous Hall effect (AHE) and planar Hall effect (PHE) resistances, respectively. Note that a linear background (first term of Equation (1)) generated from the ordinary Hall effect ($R_{OHE}$) is excluded due to its negligible magnitude in this analysis. To separate the total observed $R_H$ into a pristine Hall signal ($R_{H0}$) upon zero current and a variation in

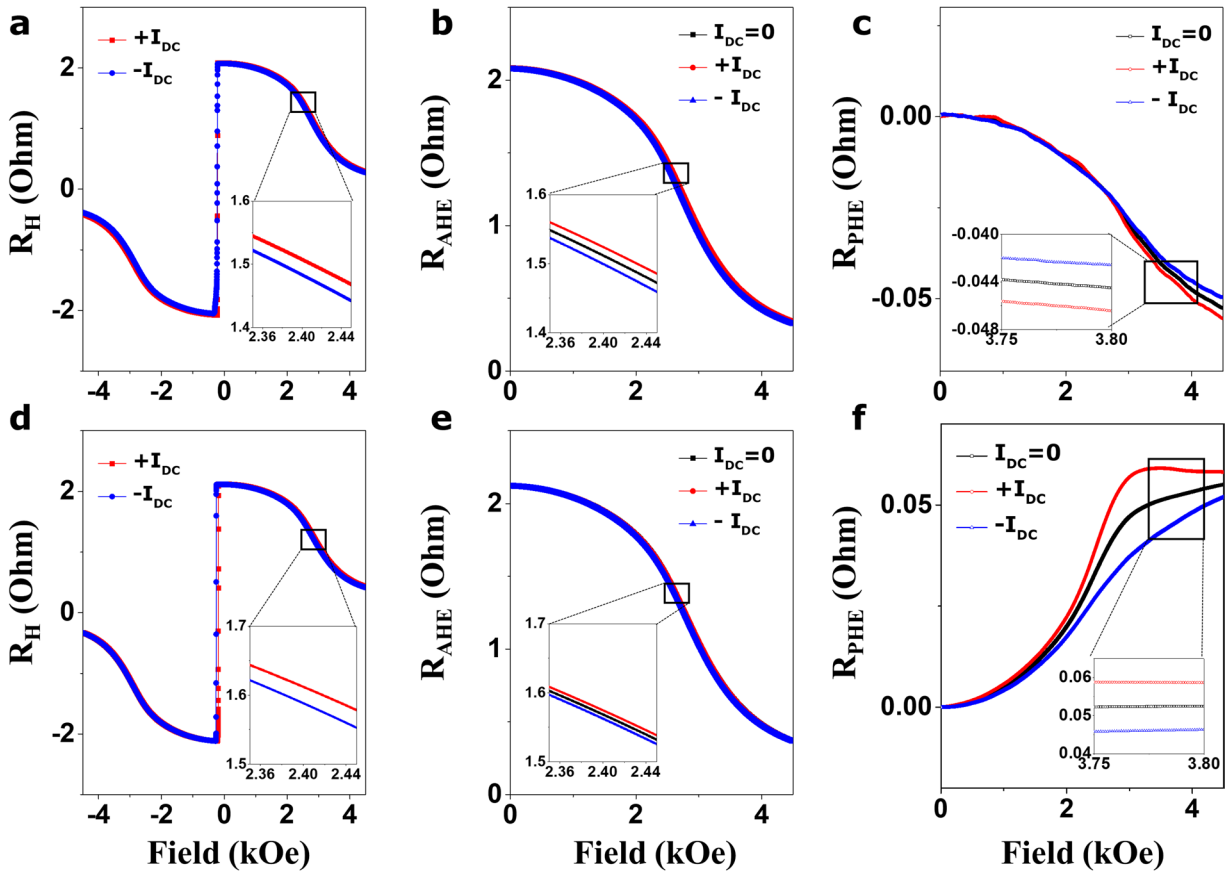


**Figure 2.** Magnetic features of the Ta-based sample [Sample A] under a DC source for two measurement schemes. (**a**) Hall resistance $R_H$ versus $H_{ext}$ parallel to the positive (red line) and negative (blue line) current $I_{dc}$ with a magnitude of 0.5 mA. (**b**,**c**) Separated anomalous Hall effect signal ($R_{AHE}$) and planar Hall effect signal ($R_{PHE}$) from the $R_H$ as a function of $H_{ext}$ parallel to zero-current (black line), +0.5 mA (red line) and −0.5 mA (blue line). (**d**) Hall resistance $R_H$ verse $H_{ext}$ perpendicular to the positive (red line) and negative (blue line) current $I_{dc}$ with a magnitude of 0.5 mA. Similarly, (**e**,**f**) $R_{AHE}$ and $R_{PHE}$ versus $H_{ext}$ perpendicular to zero-current (black line), +0.5 mA (red line) and −0.5 mA (blue line). Insets: the magnified features of the graphs reflect the obvious difference in the main curves recorded at $\pm I_{dc}$ current, which lowered the magnetization in one direction and increased it in the other direction.

the Hall resistance ($\Delta R_H$) upon the injection of $I_{dc}$ with a certain magnitude, the $R_H$ of Equation (1) was approximated using a Taylor expansion only to the first order as follows:

$$R_H(I_{dc}) \cong R_H(I_{dc} = 0) + I_{dc} \cdot \frac{dR_H}{dI}_{I=0} \equiv R_{H0} + \Delta R_H, \tag{2}$$

where the Hall resistance in the absence of $I_{dc}$ is denoted by $R_{H0} \equiv R_H(I_{dc} = 0)$, and the variation of $R_H$ by the $I_{DC}$ is $\Delta R_H$. The $R_{H0}$ and $\Delta R_H$ upon $\pm I_{dc}$ can be obtained by

$$R_{H0} = \frac{R_H(I_{dc}) + R_H(-I_{dc})}{2}, \Delta R_H = \frac{R_H(I_{dc}) - R_H(-I_{dc})}{2} \tag{3}$$

Similarly, the two AHE- and PHE-associated terms with respect to $\pm H_{ext}$ in the presence of $I_{dc}$ can be determined by the resulting expressions:

$$R_{AHE} \cdot \cos\theta = \frac{R_H(H_{ext}) - R_H(-H_{ext})}{2}, R_{PHE} \cdot \sin^2\theta \cdot \sin 2\varphi = \frac{R_H(H_{ext}) + R_H(-H_{ext})}{2}, \tag{4}$$

where detailed equations are given in Supplementary Information 1. Use of the above relations enables the determination of contributions to the total $R_H$. Figure 2b,c,e, and f plot the separated $R_{AHE}$ and $R_{PHE}$ signals of Sample A at three different $I_{dc}$ injections ($I_{dc}$ = +0.5 mA, 0, −0.5 mA) for both parallel (Fig. 2b,c) and perpendicular (Fig. 2e,f) schemes, where the plots are given only in the positive $\overrightarrow{H}_{ext}$ region due to the symmetric features in the $R_H$ curves of Fig. 2a,d. The separated $R_{AHE}$ and $R_{PHE}$ at the zero current (I = 0) are obtained by the $R_{H0}$ expression in equation (3). The insets of Fig. 2b,e show that reversing the sign of $I_{dc}$ clearly leads to the up (red line) and down

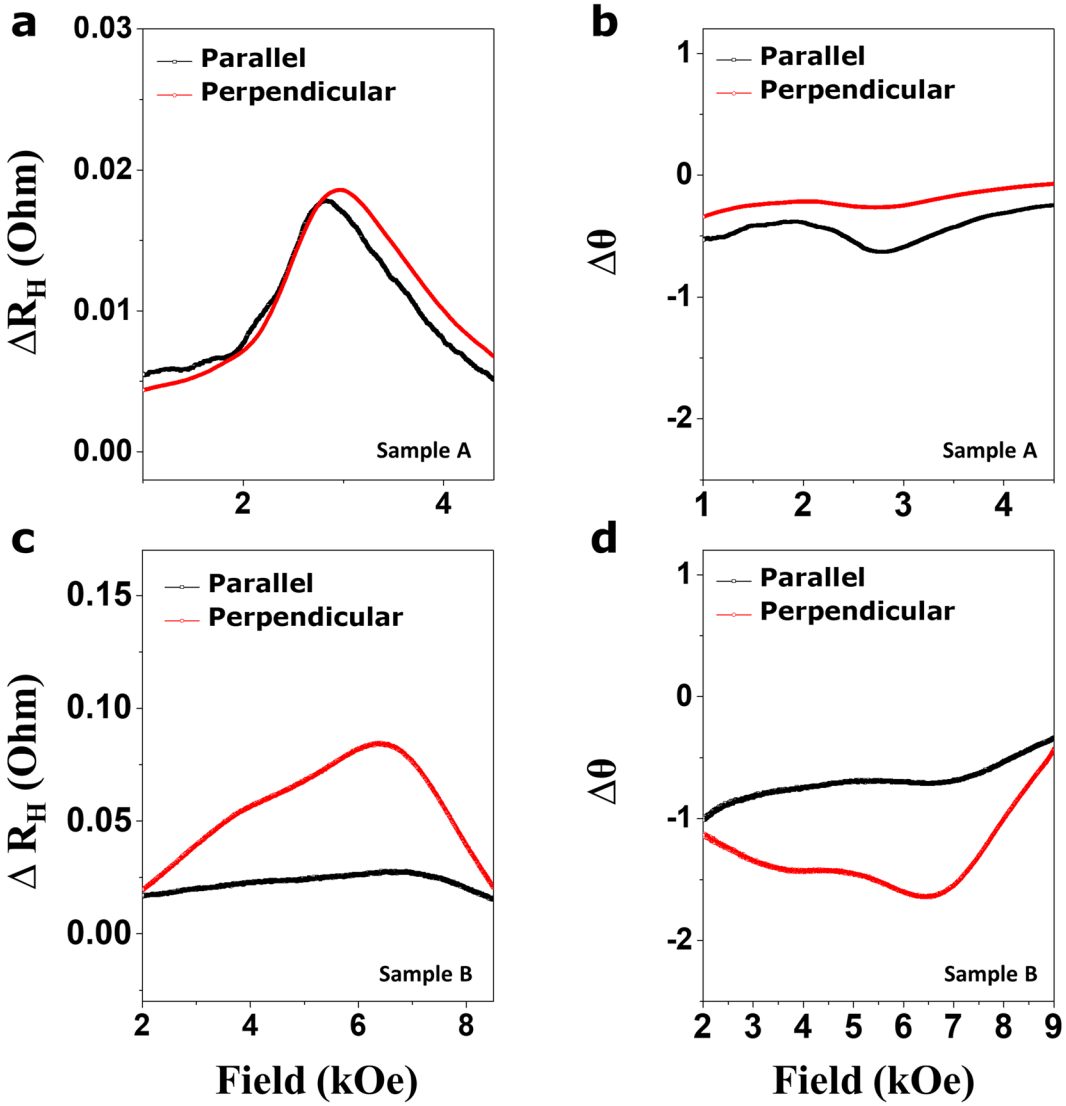


**Figure 3.** Variations in Hall resistance and polar angles for Samples A and B. (**a**,**b**) Plots of Hall resistance variation $\Delta R_H$ and polar angle change $\Delta\theta$ versus $H_{ext}$ parallel (black line) and perpendicular (red line) to the current direction for Sample A. (**c**,**d**) Similar plots of $\Delta R_H$ and $\Delta\theta$ versus $H_{ext}$ parallel (black line) and perpendicular (red line) to the current direction for Sample B, where a current of 0.5 mA was applied for both samples.

(blue line) $R_{AHE}$ curves of Sample A, along with the $R_{AHE}$ (black line) upon zero current. The insets of Fig. 2c,f show similar trends for the $R_{PHE}$ curves that are dependent on the sign of $I_{dc}$. In addition, a closer investigation of Fig. 2b,c suggests that $R_{PHE}$ is small (i.e., a factor of $10^2$ and 10 less than values of $R_{AHE}$ for Samples A and B, respectively), reflecting a slight contribution to the rotational variance around the $\varphi$ upon $I_{dc}$ application. Thus, the magnitude of $R_{PHE}$ can be used to determine current-induced effective fields only by means of the $\Delta R_{AHE}$ estimated for both schemes because the contribution of $R_{PHE}$ to the $R_H$ is negligible in our work. Similarly, the $R_H$, $R_{AHE}$, and $R_{PHE}$ trends of Sample B are similar to the observations of Sample A. More detailed plots for Sample B are presented in Fig. S2 of the Supporting Information. We believe that the determined $R_{AHE}$ and $R_{PHE}$ are primarily the consequence of magnetization tilting induced by the application of $I_{dc}$, as depicted in Fig. 1b,c.

Figure 3a,c show the variation in Hall resistance ($\Delta R_H$) for Samples A and B as a function of $H_{ext}$ in both schemes. Both samples reveal the strong dependence of $\Delta R_H$ on $H_{ext}$. As is evident in this figure, Sample B yields larger $\Delta R_H$ and $\Delta\theta$ than those of Sample A, possibly reflecting the presence of the large SOT initially created by the W buffer layer during growth or annealing compared to the Ta buffer layer. The possible presence of larger SOTs in Sample B (W-based frame) could be linked to both the large spin Hall angle (SHA) that is initially present in a highly resistive β-phase W layer or the extrinsic SHE nature of the sample. To illustrate the SHA contribution to the larger SOT, numerous studies have addressed the presence of the extraordinary large SHA in the β-phase W ($\theta_{SH}^{\beta-W}$), which was 2 times[19] or almost 4 times[20] larger than those in the β-phase Ta ($\theta_{SH}^{\beta-Ta}$). In addition, Demasius *et al.*[21] have also reported the enhancement of SOT by controlling the oxygen concentration in the β-W film. These works suggest the possibility of a large SHA value in β-W by considering the special microstructure

(A15) of β-W, while the α-phase W with a BCC structure is expected to have a smaller SHA value. Thus, the use of the β-phase W buffer layer in Sample B corresponds to the presence of a large SOT in our work (see the XRD analysis given in Supplementary Information 4 and the determined resistivity 172 μΩ·cm, 139 μΩ·cm for Ta and W, respectively). Secondly, it is widely believed that three main mechanisms have a significant impact on the SHE dynamics: an intrinsic mechanism, skew scattering, and side-jump scattering. The last two scattering terms are the so-called extrinsic mechanism, where the scattering sources are likely to arise from impurities or defects generated mainly in the HMs. In general, post annealing is a generic approach for the formation of well-aligned crystalline regions through boron out-diffusion from the CoFeB FM layer. This process ensures that the interface PMA features operate reliably to meet the demand of PMA-based devices. Thus, thermal annealing of Samples A and B lets thermally-activated B ions diffuse toward the HM layer or thermally-activated Ta or W ions migrate toward the FM layer, causing atomic intermixing of the layers[22]. According to recent work[23], a heavy metal dopant on the ferromagnet resulted in an enhancement in SOI. In this regard, annealing results in suitable atomic mixing with Co, Fe, B, HM, or oxygen atoms in an FM or HM layer, reflecting the presence of an enhanced SOI-driven SHA in Sample B. Third, the different crystalline states observed within the two Ta and W buffer layers are also related to the SOI features. The Ta buffer layer exhibits a nearly β-phase structure, while the W buffer layer reveals a A15 crystalline structure after annealing (See XRD analysis given in Supplementary Information 4 and the determined resistivity of 172 μΩ·cm, 139 μΩ·cm for Ta and W, respectively). Therefore, HM and FM can include different defects or impurities after annealing. Finally, the affinity of B for the Ta and W buffer layers can likely help reduce the amount of defects or impurities within the HMs since B diffusion is different even at the same annealing temperature[24]. Figure 3a,c also show that a relatively large $\Delta R_H$ occurs at around 3 kOe for Sample A and 6 kOe for Sample B, in which fields of 3 and 6 kOe are very close to the anisotropy fields ($H_k$) of Samples A and B, respectively (see Supplementary Information 3). Similarly, Fig. 3b,d show the change in magnetization polar angle (Δθ) induced by the positive current (+0.5 mA) injection, which is determined from the two separated AHE signals (I = 0, +0.5 mA) for Samples A and B. A relatively large Δθ in both samples also becomes obvious in the vicinity of the $H_k s$. Thus, the similarities in peaks of $\Delta R_H$ and Δθ in the vicinity of the $H_k s$ implies that their natures are similar regardless of whether the Ta or W buffer layer is used. However, the peak behavior in the vicinity of the $H_k s$ for Samples A and B is not clearly understood at present.

Differences in Δθs are commonly caused by variations in the magnitudes of $H_f$ and $H_d$, which are separately determined from the parallel and perpendicular schemes. As displayed in Fig. 3b,d, the $H_{ext}$-dependency of Δθ implies that the magnitude of the current-induced torques is not constant with regard to $H_{ext}$ or θ. In this sense, the specific dependence of θ on the magnitudes of $H_f$ and $H_d$ can be obtained from the observed Δθ traces to further explore the nature for the SOTs in the FM layer. Thus, to derive the magnitude of each $H_f$ and $H_d$ from the observed θ, the total magnetic energy of a perpendicularly magnetized system with the injected current can be expressed as

$$E = -K_{eff}\cos^2\theta - \vec{M}\cdot\vec{H}_{tot} \tag{5}$$

Here, $\vec{H}_{tot} \equiv \vec{H}_{ext} + \vec{H}_f + \vec{H}_d$, where $\vec{H}_f \equiv H_f\vec{\sigma}$, $\vec{H}_d \equiv H_d(\hat{M}\times\vec{\sigma})$, $\vec{H}_{ext}$ is an external magnetic field, $\vec{\sigma}$ is the spin direction of spin-polarized electron, s and $\vec{M}$ is magnetization of an FM layer. Under this condition, the $H_d$ and $H_f$ from each schemes are given by[15,25]

$$H_d = \Delta\theta(H_k\cos 2\theta_0 + H_{ext}\cos(\theta_H - \theta_0)) \tag{6}$$

$$H_f = [\Delta\theta(H_k\cos 2\theta_0 + H_{ext}\cos(\theta_H - \theta_0)]/\cos\theta_0. \tag{7}$$

where $H_k$ is the anisotropy field $\left(H_k \equiv \frac{2K_{eff}}{M_s}\right)$. A more detailed description of the above equations is given in Supplementary Information 1.

Figure 4 exhibits the θ-dependence of $H_d$ and $H_f$ for Samples A (Fig. 4a,b) and B (Fig. 4c,d) under positive (black) and negative (red) $I_{dc}$. Plots of Sample A present the typical behaviors in sign and magnitude observed from the previously reported works[11,12,26], where the representatively reported average magnitudes of $H_d$ and $H_f$ for Sample A are ~20 Oe/MA·cm$^{-2}$, which corresponds to the obtained values from the typical harmonic analysis for Sample A (blue spheres). As harmonic signal-based analysis cannot be applied to W-based samples[27], harmonic analysis for Sample B has not been carried out. In addition, the amplitude of $H_d$ of Sample A is always larger than that of the $H_f$ over the whole θ range ($H_d > H_f$). This is similar to previously reported works (~2 times larger)[14]. However, such a trend is reversed in Sample B, where the amplitude of $H_f$ is always larger than that of $H_d$ in the full θ range ($H_d < H_f$). The dissimilarities in Samples A and B imply that their natures are also dissimilar, i.e., the SHE and Rashba contributions to the $H_d$ and $H_f$ are different for each material. Based on previous studies[12], we expect two major contributions to the dissimilarities of Samples A and B, respectively. First, if the relatively large SHE for Sample B is assumed to arise from β-phase W or suitable impurities or defects, a larger SHA value of about 0.3 for Sample B allows efficient generation of a more abundant spin current $\left(\vec{J}_s = \theta_{SH}\cdot\frac{\hbar}{2e}\cdot\vec{J}_c\times\vec{\sigma}\right)$, ultimately reflecting larger $H_d$ and $H_f$ values for Sample B even at the same current injection. In addition, the presence of relatively higher resistance in W buffer layer may be associated with the particularly enhanced Hf component of Sample B. The recent theoretical work 28 has suggested that the field-like torque can significantly be affected by the current flowing inside an FM layer with a 2D Rashba model or SHE model. In this sense, the W buffer layer that can absorb more boron and oxygen atoms during growth or annealing possibly creates a higher resistance than that of the Ta layer (See Supplementary Information S9), thus

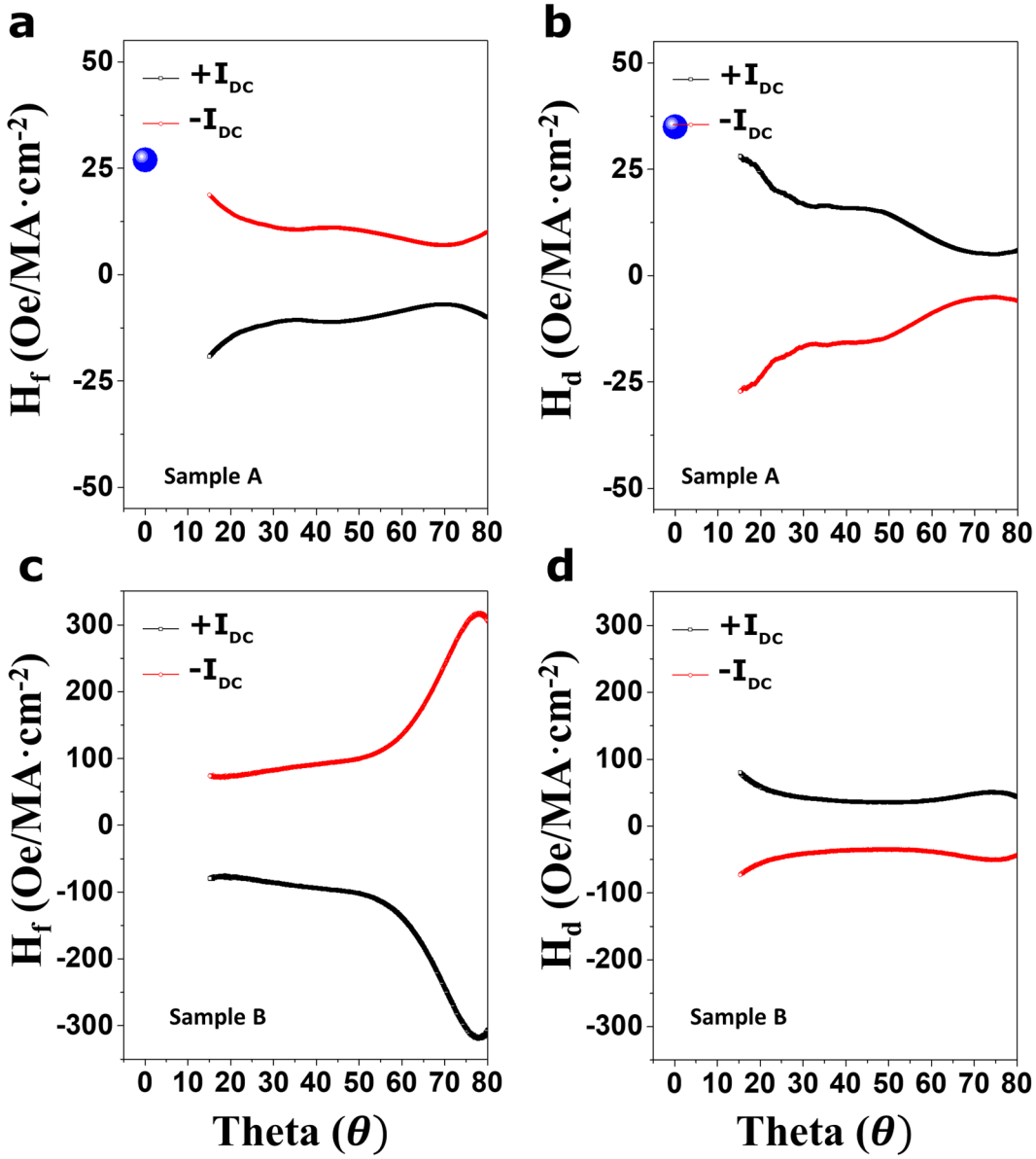


**Figure 4.** Angular dependence traces of current-driven $H_d$ and $H_f$ components. Each component of the current-induced effective fields was calculated from the parallel and perpendicular configurations for Samples A and B. Plots of the $H_f$ components versus θ under positive (black line) and negative currents (red line) for (**a**) Sample A and (**c**) Sample B. Plots of the $H_d$components versus θ for (**b**) Sample A and (**d**) Sample B. The corresponding results reflect the strong angular dependency of $H_f$ and $H_d$ components, where the applied magnitude of the current was 0.5 mA. Blue spheres indicate the obtained data from typical harmonic analysis.

providing the remarkably enhanced Hf component in Sample B. The values of Hdand Hf reveal a strong θ dependence, as evident in the above equation and the empirical results of Fig. 4. However, questions remain regarding why there is an abnormal angular dependence of both components over the full θ range. In addition, the experimental observations cannot be completely described by either the SHE or Rashba model. The unclear θ-dependent phenomena observed in the full θ range are likely linked to a combination of two apparent dynamics, along with unknown additional structural contributions. Recent theoretical works[12,14,15,29] addressed the θ-dependent behaviors of spin-orbit torque without identifying their origins. For example, the bulk SHE-based theories combined with the Boltzmann equation and a simpler drift-diffusion approach[30] predicted no angular dependence of either Hf or Hd. On the other hand, the interfacial Rashba-based theories in a strong Rashba effect regime (compared to the exchange coupling strength[31]) showed a strong angular dependence of Hd through the anisotropy of the spin relaxation. However, Hf remains almost constant even after introduction of spin relaxation anisotropy. Thus, the θ dependence of diverse Hd and Hf reported by numerous studies[12,14,15,29] (including our work) showed less agreement with the currently available theoretical models. Thus, attaining a firm understanding of the physical nature of these systems is still a major challenge that must be addressed to extend their use. Overall, a clearer model for the origin of current-induced effective fields observed in the samples must be developed.

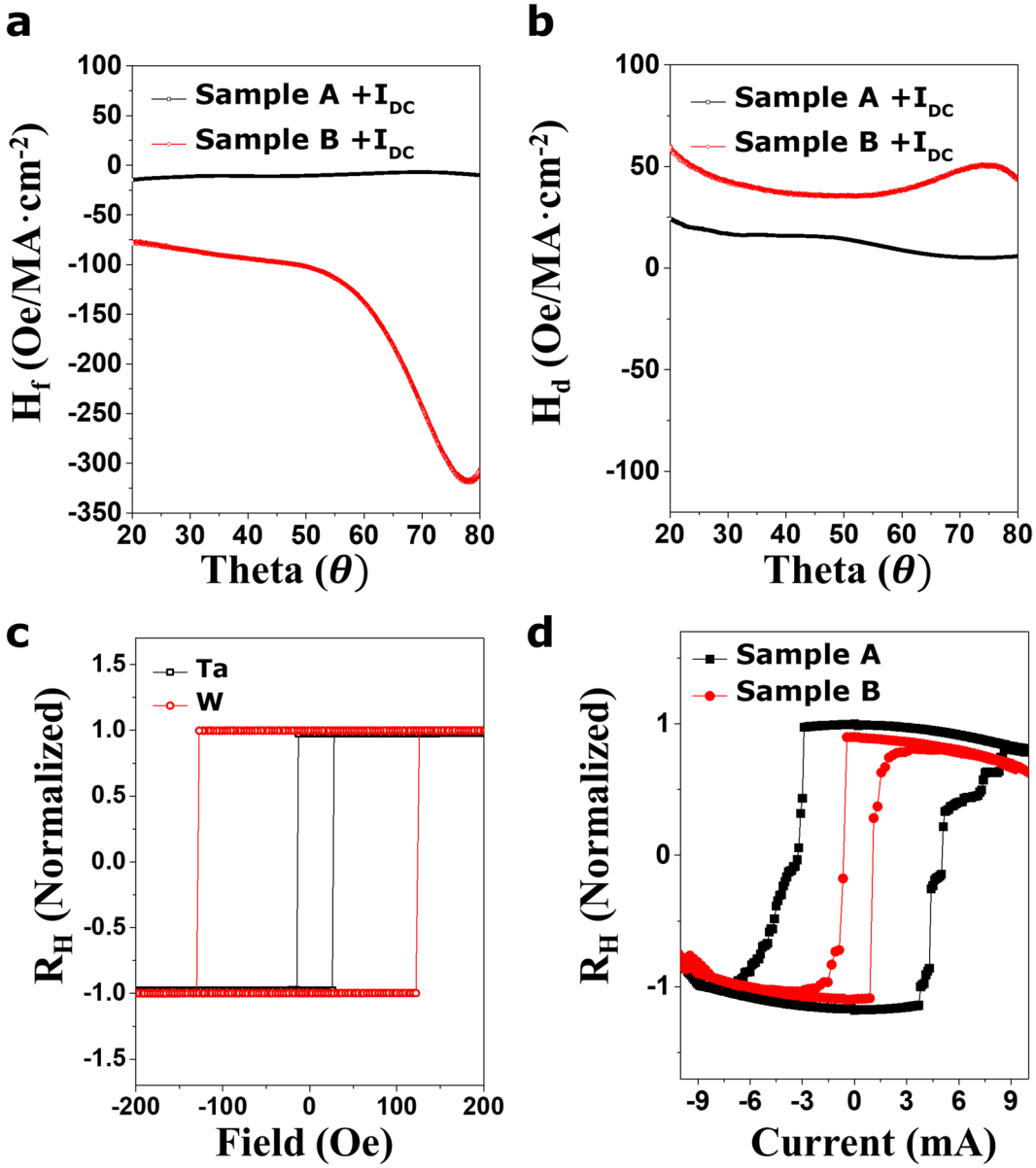


**Figure 5.** Comparison of $H_d$ and $H_f$ components and current-induced switching behavior for Samples A and B. (**a**) $H_f$ and (**b**) $H_d$ versus θ are plotted upon positive injection of +0.5 mA for Sample A (black lines) and B (red lines). Samples A and B always display relatively dominant $H_f$ and $H_d$ trends in the magnitude over the entire θ range, respectively. That is, the dissimilarity in the effective field characteristics of Samples A and B implies that the natures of the Ta and W HM layers are also inherently dissimilar. The clear enhancement in $H_d$ for Sample B indicates the improved spin Hall angle, especially in Sample B (W-based sample). (**c**) The anomalous Hall resistance with out-of-plane field for Sample A and B. (**d**) Current switching with the external field of 50 Oe along the current direction for sample A and B. The normalized Hall resistance ($R_H$) is plotted with the injected current for sample A (Black line) and sample B (Red line). The lower switching current is clearly observed for sample B case.

Figure 5 shows a plot the $H_f$ (Fig. 5a) and $H_d$ (Fig. 5b) of Samples A (black line) and B (red line) as a function of θ to emphasize the difference in magnitude of the current-induced effective fields. Experiments showed that the magnitude of $H_d$ and $H_f$ for Sample B was about 10 times ($H_f$) and 2 times ($H_d$) larger over the whole θ region. This increase in $H_d$ and $H_f$ magnitude for Sample B can be ascribed to the enhanced bulk-SHE or the current in an FM layer, as explained in Fig. 4 section. Given the important features of $H_d$, the spin Hall angles (SHA, $\theta_{SH}$) for Samples A and B are calculated by $H_d = -\frac{\hbar}{2e} \cdot \frac{J_{HM}}{\mu_0 M_s d_{FM}} \cdot \theta_{SH}$, here, $\hbar$ is the reduced Planck constant: $1.054 \times 10^{-34}\ J \cdot s$, e is the elementary charge: $1.602 \times 10^{-19}$ C, $J_{HM}$ is the current density through the HM: $5 \times 10^{10} A/m^{-2}$, $\mu_0$ is the permeability of free space: $1.256 \times 10^{-6}\ N \cdot A^{-2}$, $M_s$ is the saturation magnetization: $1.203 \times 10^6 A/m$ for Sample A and $1.259 \times 10^6 A/m$ for Sample B, and $d_{FM}$ is the effective magnetic layer thickness corrected by considering magnetic dead layers (see Supplementary Information 7): $0.8 \times 10^{-9}$ m for both samples. The calculated SHAs for Samples A and B are given in Figure S6. The determined SHA values (Ta $\sim -0.1$, W $\sim -0.3$) are comparable with

those in previous papers[20]. The enhancement of SHA arising from the β-phase W is clearly observed as expected. This feature can also be confirmed in the current switching behaviors for both samples. As seen in Fig. 5d, both samples with the identical FM thicknesses exhibit different switching currents: ~$3 \times 10^7$ A/cm$^{-2}$ for sample A, ~$1 \times 10^7$ $A/cm^{-2}$ for sample B. These switching current values are approximately well-matched with the relative magnitudes of $H_d$ values observed from both samples (2 times larger in Sample B) because the current-induced magnetization switching is dominantly operated by the damping-like component[1]. However, the θ–dependent SHAs are still unclear. As seen in Fig. 5d, both samples with the identical FM thicknesses exhibit different switching currents: ~$3 \times 10^7$ A/cm$^{-2}$ for sample A and ~$1 \times 10^7$ $A/cm^{-2}$ for sample B. These switching current values are approximately well-matched with the relative magnitudes of $H_d$ values observed from both samples (2 times larger in Sample B) because the current-induced magnetization switching is dominantly operated by the damping-like component. Since the intrinsic SHA value in the bulk HM does not rely on θ, the transparency of spin current injected into the FM layer at the HM/FM interface might be a possible origin of the variation in effective SHA ($\theta_{SH}^{eff}$). To give rough estimates for the strong θ-dependent SHA, a brief interfacial spin-dependent scattering concept in a particular high θ regime is provided as proof of the possible nature. Zhang *et al.*[32] have addressed that the interfacial transparency of spin current can be associated with the spin-mixing conductance, which is a function of magnetic damping constant. In addition, W. Kim *et al.*[33] reported the angle-dependent magnetic damping constant possibly induced by the spin pumping effect. This paper pointed out the decrease in damping constant as the θ increased. Thus, the decreased damping constant can reduce the transparency of spin current at the interface when the following equation is used

$$T = \frac{G_{\uparrow\downarrow} \tanh\left(\frac{d_{HM}}{2\lambda}\right)}{G_{\uparrow\downarrow} \coth\left(\frac{d_{HM}}{\lambda}\right) + \frac{\sigma_{HM}}{\lambda}\frac{h_{HM}}{2e^2}}, \tag{8}$$

where $G_{\uparrow\downarrow}$ is the spin-mixing conductance, λ is the spin diffusion length, $\sigma_{HM}$ is the conductivity of heavy metals, $h_{HM}$ is Planck's constant and $d_{HM}$ is the thickness of heavy metals. This models may explain the reduction in the effective SHA and the corresponding $H_d$ as the θ increases. In addition, using Zhang's initial transparency concept, another feasible scenario for the transparency could be as follows: if the injected spin current pointing along the y-axis exchanges with a total angular momentum ($\vec{J}$) in d orbitals of an adjacent FM, the spin current transparency at the interface is also affected by the θ of FM when the θ-dependent barrier height is present at the interface. In this scenario, the $H_d$ in a parallel scheme is not relevant to the θ dependence since the spin current injected along the y-axis is always perpendicular to the magnetization direction in a parallel scheme. The corresponding exchange interaction is equal for all magnetization polar angles. However, the $H_f$ in a perpendicular scheme also has θ dependence due to the presence of $-J_{ex}\vec{M} \cdot \vec{\sigma}$, where $\vec{\sigma}$ is directed along the y-axis. Thus, since movement toward the high θ regime allows the magnetization direction to primarily be close to the y-axis, the electron in the spin current will experience fewer scattering events due to the further reduced energy barrier. Such an event results in a spin current with large transparency, which facilitates injection of spin current. As a result, the $H_f$is enhanced with an increase in θ, as seen in the high θ region of Fig. 4a,c. The angular dependence of $H_f$ in the high θ region can be expressed by the transparency concept. However, the abnormal decrease in higher θ (>75°) and the behavior in the middle range θ (20° ∼ 60°) of both samples still remains a challenge so that a new physics beyond the currently available models should be established.

## Conclusions

In summary, in-plane DC measurements of spin-orbit torque components in Ta- and W-based CoFeB/MgO frames are employed as an independent analysis tool to examine the in-plane current-induced magnetization switching. The observed spin-orbit torque components for the two frames reveal a strong dependence on the magnetization of the polar angles. In particular, relatively larger Rashba and spin Hall dynamics are the dominant contributions to Samples A and B, respectively. Identifying the underlying nature of these phenomena remains a key challenge toward extending the use of these materials. One possible nature is the interfacial spin-dependent scattering arising from the exchange interactions between the angular momentum of d electrons in the CoFeB layer and the spin state of conduction electrons in the heavy metal layer. We anticipate that the study of this simple DC approach will open a suitable path to explore new physical phenomena and provide low power and high speed spin-orbit torque-based spintronic devices.

## Methods

The stacks used in this work were deposited on thermally oxidized Si substrates utilizing magnetron sputtering with a base pressure $<2 \times 10^{-8}$ Torr at room temperature. Species were as follows: [Si/$SiO_2$(200)] substrate/heavy metals (5)/$Co_{20}Fe_{60}B_{20}$ ($t_{CFB}$)/MgO (1)/Ta (2), where the numbers in parentheses refer to the layer thickness in nanometers, and the heavy metals are Ta (Sample A) and W (Sample B). To promote perpendicular magnetic anisotropy (PMA) features, a post-annealing process was carried out at 250 °C (Sample A) and 300 °C (Sample B) for 1 hour under vacuum conditions below ~$1 \times 10^{-6}$ Torr with a 3 Tesla perpendicular magnetic field for all samples investigated here. The deposited stacks were spin-coated with AZ5214E image reversal photoresist and patterned into 10 μm width Hall bars by photolithography and Ar ion milling. Acetone was used to lift off the photo resist. Oxygen plasma etching was carried out for 2 minutes with 50 Watt RF power to remove residual photoresist hardened during the ion-milling process. The Hall channel contacts were defined by photolithography followed by the deposition of W (50 nm) and were connected to the Hall bars. Devices were wire-bonded to the sample holder using indium balls and were installed in a home-made electrical probing system with a ~1 Tesla electromagnet using a Keithley 236 source measure unit and Hewlett Packard 34401A multi-meter devices[34].

## References


1. Qiu, X. *et al*. Spin-orbit-torque engineering via oxygen manipulation. *Nat. Nanotechnol.* **10**, 333–338 (2015).
2. Miron, I. M. *et al*. Perpendicular switching of a single ferromagnetic layer induced by in-plane current injection. *Nature* **476**, 189–193 (2011).
3. Liu, L. *et al*. Spin-Torque Switching with the Giant Spin Hall Effect of Tantalum. *Science* **336**, 555–558 (2012).
4. Oh, Y.-W. *et al*. Field-free switching of perpendicular magnetization through spin–orbit torque in antiferromagnet/ferromagnet/oxide structures. *Nat. Nanotechnol.* **11**, 878–884 (2016).
5. Bhowmik, D., You, L. & Salahuddin, S. Spin Hall effect clocking of nanomagnetic logic without a magnetic field. *Nat. Nanotechnol.* **9**, 59–63 (2014).
6. Ryu, K.-S., Thomas, L., Yang, S.-H. & Parkin, S. Chiral spin torque at magnetic domain walls. *Nat. Nanotechnol.* **8**, 527–533 (2013).
7. Emori, S., Bauer, U., Ahn, S.-M., Martinez, E. & Beach, G. S. D. Current-driven dynamics of chiral ferromagnetic domain walls. *Nat. Mater.* **12**, 611–616 (2013).
8. Liu, L., Pai, C.-F., Ralph, D. C. & Buhrman, R. A. Magnetic Oscillations Driven by the Spin Hall Effect in 3-Terminal Magnetic Tunnel Junction Devices. *Phys. Rev. Lett.* **109**, 186602 (2012).
9. Miron, I. M. *et al*. Current-driven spin torque induced by the Rashba effect in a ferromagnetic metal layer. *Nat. Mater.* **9**, 230–234 (2010).
10. Wang, X. & Manchon, A. Diffusive Spin Dynamics in Ferromagnetic Thin Films with a Rashba Interaction. *Phys.l Rev. Lett.* **108**, 117201 (2012).
11. Kim, J. *et al*. Layer thickness dependence of the current-induced effective field vector in Ta|CoFeB|MgO. *Nat. Mater.* **12**, 240–245 (2013).
12. Garello, K. *et al*. Symmetry and magnitude of spin-orbit torques in ferromagnetic heterostructures. *Nat. Nanotechnol.* **8**, 587–593 (2013).
13. Liu, L., Lee, O. J., Gudmundsen, T. J., Ralph, D. C. & Buhrman, R. A. Current-induced switching of perpendicularly magnetized magnetic layers using spin torque from the spin Hall effect. *Phys. Rev. Lett.* **109**, 096602 (2012).
14. Qiu, X. *et al*. Angular and temperature dependence of current induced spin-orbit effective fields in Ta/CoFeB/MgO nanowires. *Sci. Rep.* **4**, 4491 (2014).
15. Chen, Y. *et al*. Quantifying angular dependence of spin-orbit torques in Ta/CoFeB/MgO trilayers with perpendicular magnetic anisotropy. *Phys. Rev. B* **95**, 144405 (2017).
16. Kawaguchi, M. *et al*. Current-Induced Effective Fields Detected by Magnetotrasport Measurements. *Appl. Phys. Exp.* **6**, 113002 (2013).
17. Han, J. *et al*. Room-Temperature Spin-Orbit Torque Switching Induced by a Topological Insulator. *Phys. Rev. Lett.* **119**, 077702 (2017).
18. Ikeda, S. *et al*. A perpendicular-anisotropy CoFeB–MgO magnetic tunnel junction. *Nat. Mater.* **9**, 721–724 (2010).
19. Pai, C.-F. *et al*. Spin transfer torque devices utilizing the giant spin Hall effect of tungsten. *Appl. Phys. Lett.* **101**, 122404 (2012).
20. Qu, D., Huang, S. Y., Miao, B. F., Huang, S. X. & Chien, C. L. Self-consistent determination of spin Hall angles in selected $5d$ metals by thermal spin injection. *Phys. Rev. B* **89**, 140407 (2014).
21. Demasius, K.-U. *et al*. Enhanced spin–orbit torques by oxygen incorporation in tungsten films. *Nat. Commun.* **7**, 10644 (2016).
22. An, G.-G. *et al*. Highly stable perpendicular magnetic anisotropies of CoFeB/MgO frames employing W buffer and capping layers. *Acta. Mater.* **87**, 259–265 (2015).
23. Hrabec, A. *et al*. Spin-orbit interaction enhancement in permalloy thin films by Pt doping. *Phys. Rev. B* **93**, 014432 (2016).
24. Niessen, A. K. & De Boer, F. R. The enthalpy of formation of solid borides, carbides, nitrides, silicides and phosphides of transition and noble metals. *J. Alloy. Compd.* **82**, 75–80 (1981).
25. Hayashi, M., Kim, J., Yamanouchi, M. & Ohno, H. Quantitative characterization of the spin-orbit torque using harmonic Hall voltage measurements. *Phys. Rev. B* **89**, 144425 (2014).
26. Cecot, M. *et al*. Influence of intermixing at the Ta/CoFeB interface on spin Hall angle in Ta/CoFeB/MgO heterostructures. *Sci. Rep.* **7**, 968 (2017).
27. Torrejon, J. *et al*. Interface control of the magnetic chirality in CoFeB/MgO heterostructures with heavy-metal underlayers. *Nat. Commun.* **5**, 4655 (2014).
28. Kim, K.-W., Lee, K.-J., Sinova, J., Lee, H.-W. & Stiles, M. D. Spin-orbit torques from interfacial spin-orbit coupling for various interfaces. *Phys. Rev. B* **96**, 104438 (2017).
29. Schulz, T. *et al*. Effective field analysis using the full angular spin-orbit torque magnetometry dependence. *Phys. Rev. B* **95**, 224409 (2017).
30. Haney, P. M., Lee, H.-W., Lee, K.-J., Manchon, A. & Stiles, M. D. Current induced torques and interfacial spin-orbit coupling: Semiclassical modeling. *Phys. Rev. B* **87**, 174411 (2013).
31. Lee, K.-S. *et al*. Angular dependence of spin-orbit spin-transfer torques. *Phys. Rev. B* **91**, 144401 (2015).
32. Zhang, W., Han, W., Jiang, X., Yang, S.-H. & Parkin, S. P. S. Role of transparency of platinum-ferromagnet interfaces in determining the intrinsic magnitude of the spin Hall effect. *Nat. Phys.* **11**, 496–502 (2015).
33. Kim, W. J., Lee, T. D. & Lee, K. J. Effect of the Angle-Dependent Gilbert Damping Constant on the Magnetization Dynamics Induced by a Spin Polarized Current. *IEEE. Trans. Magn.* **42**, 3207–3209 (2006).
34. Yu, G. *et al*. Switching of perpendicular magnetization by spin-orbit torques in the absence of external magnetic fields. *Nat. Nanotechnol.* **9**, 548–554 (2014).


## Acknowledgements

This research was supported by Nano-Material Technology Development Program through the National Research Foundation of Korea (NRF) funded by Ministry of Science and ICT (NRF-2016M3A7B4910249).

## Author Contributions

J.H. supervised the study, and S.Y. and J.H. prepared the design and wrote the main manuscript. The experiments and analysis were carried out by S.Y, while J.C., J.S., K.Y., J.Y. discussed the manuscript during preparation. All authors discussed the results and reviewed the manuscript.

## Additional Information

**Supplementary information** accompanies this paper at https://doi.org/10.1038/s41598-018-29397-4.

**Competing Interests:** The authors declare no competing interests.

**Publisher's note:** Springer Nature remains neutral with regard to jurisdictional claims in published maps and institutional affiliations.